Structural and luminescence investigation on gadolinium gallium garnet nanocrystalline powders prepared by solution combustion synthesis

To cite this article: R Krsmanovi *et al* 2007 *Nanotechnology* **18** 325604

IOP PUBLISHING NANOTECHNOLOGY
Nanotechnology **18** (2007) 325604 (9pp) doi:10.1088/0957-4484/18/32/325604

Structural and luminescence investigation on gadolinium gallium garnet nanocrystalline powders prepared by solution combustion synthesis

R Krsmanović[1,5], V A Morozov[2], O I Lebedev[1], S Polizzi[3], A Speghini[4], M Bettinelli[4] and G Van Tendeloo[1]

[1] EMAT, University of Antwerp, Groenenborgerlaan 171, B-2020 Antwerp, Belgium
[2] Department of Chemistry, Moscow State University, 119899 Moscow, Russia
[3] Department of Physical Chemistry, Ca' Foscari University of Venice, Via Torino 155/b, I-30172 Venice, Italy
[4] Dipartimento Scientifico e Tecnologico, University of Verona and INSTM, UdR Verona, Ca' Vignal, Strada Le Grazie 15, I-37134 Verona, Italy

E-mail: radenka@vin.bg.ac.yu

Received 12 March 2007, in final form 30 May 2007
Published 13 July 2007
Online at stacks.iop.org/Nano/18/325604

Abstract
Nanocrystalline powders of undoped and lanthanide (Pr^{3+}, Tm^{3+})-doped gadolinium gallium garnet, $Gd_3Ga_5O_{12}$ (GGG), were prepared by propellant synthesis and studied by x-ray powder diffraction (XRD), electron diffraction (ED), high-resolution electron microscopy (HREM) and luminescence spectroscopy. The x-ray diffraction patterns of the GGG samples were analysed using the Rietveld method. The Rietveld refinement reveals the existence of two garnet-type phases: both are cubic (space group $Ia\bar{3}d$) with a slightly different lattice parameter and probably a slightly different composition. Electron diffraction and electron microscopy measurements confirm the x-ray diffraction results. EDX measurements for lanthanide-doped samples show that stable solid solutions with composition $Gd_{3-x}Ln_xGa_5O_{12}$, $x \approx 0.3$ (Ln = Pr; Tm) have been obtained. The luminescence properties of the Tm^{3+}-doped nanocrystalline GGG samples were measured and analysed.

1. Introduction

Lanthanide-doped gadolinium gallium oxide of composition $Gd_3Ga_5O_{12}$ (GGG) with a garnet-type ($Ca_3Al_2(SiO_4)_3$ [1]) structure is an important optical material. Compounds with a garnet-type structure usually crystallize in a cubic symmetry (space group $O_h^{10} = Ia\bar{3}d$). Nevertheless, possible distortions of the garnet structure are known [2, 3]. The $Ca_3Al_2(SiO_4)_3$ garnet structure is made up of [CaO_8] polyhedra, [AlO_6] octahedra and [SiO_4] tetrahedra. The constituent rare-earth (RE) elements in $RE_3Ga_5O_{12}$ garnets occupy the Ca positions in the $Ca_3Al_2(SiO_4)_3$ structure while the gallium cations are located in octahedral and tetrahedral sites. The crystal growth of GGG, carried out with the Czochralski method, produces excellent colourless single crystals, with a high melting point (1750 °C) and a density of 7.08 g cm^{-3}. The GGG lattice is body-centred cubic (bcc) with space group $O_h^{10} = Ia\bar{3}d$ and a lattice parameter of ≈1.24 nm. It has a high bulk refractive index ($n = 2$) and a transparency range from 400 to 7000 nm. It is also a very good host for doping with rare-earth ions. All these properties make doped or undoped GGG crystals very suitable for numerous technological applications, for instance as substrates for yttrium iron garnet (YIG) and YIG-like magneto-optical films [4–6] and as materials for solid-state lasers [7, 8].

Nanocrystalline GGG doped with rare earths is also an important luminescent material. It belongs to the group of

[5] Present address: Laboratory for Radiation Chemistry and Physics, Institute of Nuclear Sciences 'Vinca', PO Box 522, 11001 Belgrade, Serbia.

oxide phosphors that are optimal for field-emission display (FED) and plasma panel display (PDP) devices [9–11]. As the demands for new displays with better resolution and increased luminous efficiency are high, the display industry needs efficient nanocrystalline luminescent materials. The new phosphors have to be thermally stable, highly luminescent, radiation resistant and single phase with a small particle size. Such materials are also very efficient in infrared (IR)-to-visible up-conversion with possible applications as IR-sensitive phosphors, biological labels and up-converting materials. The appearance of many different synthesis techniques like pulsed laser deposition [12], solution combustion (propellant) [13–17], sol–gel [18], sol–gel combustion [19], wet chemical [20] or co-precipitation [21, 22] synthesis enables the production of different nanophosphors with improved characteristics. One of the advantages of these techniques is that nanocrystalline powders are obtained as a final product. Hence there is no need to use grinding or milling processes, used conventionally for the commercial phosphors with larger, micrometre-size particles. Such mechanical treatments are known to introduce surface defects and add impurities. Surface defects might cause non-radiative relaxations of the excited states and thus drastically decrease the luminescence efficiency of the phosphor. The luminescence efficiency will also decrease if dopant ions are concentrated on the nanocrystal surface or on the grain boundaries [9].

The luminescence properties of GGG single crystals doped with trivalent lanthanide ions have been studied in detail [7, 8, 23–25]. In recent years it has been shown that nanocrystalline lanthanide-doped GGG samples, obtained by the propellant technique, have very interesting luminescence properties [26–29]. In particular, intense up-conversion luminescence in the visible region is observed upon excitation with IR radiation. Moreover, the up-conversion processes are more efficient in lanthanide-doped GGG than in Y_2O_3 or Lu_2O_3 prepared with the same synthesis technique. This was explained by a much lower concentration of adsorbed contaminants (carbonate and hydroxide ions) on the surface of the GGG nanocrystals [26, 27] with respect to Y_2O_3 or Lu_2O_3 nanocrystalline materials.

Even though it has been shown that microstructural parameters such as size and surface of the nanocrystals, level of agglomeration, activator concentration and presence of defects are responsible for the luminescence efficiency of the nanocrystalline phosphors [13, 14, 18, 30–33], only a few detailed structural characterizations have been reported [17, 22, 23, 34, 35]. In our previous work [36] we studied a series of GGG samples, obtained via solution combustion synthesis, doped with different lanthanide ions (Tm, Er, Ho, Eu, Sm, Nd, Pr) and with different concentrations (1, 5, 10 mol%). For all samples XRD analysis revealed the presence of the cubic GGG phase. Each peak of the cubic GGG phase was accompanied by a weak asymmetric peak shifted to lower 2θ values. The presence of these asymmetric peaks cannot be explained as an effect of microstrains, as their value is low (of the order of 10^{-3}), but it is more likely attributed to the existence of a second phase. The regular appearance of the asymmetric peaks in all samples suggests that highly reproducible solid solutions of GGG are obtained with the propellant technique.

In this work a more detailed investigation on the structure, morphology and composition of undoped, and Pr^{3+}- or Tm^{3+}-doped GGG nanocrystalline powders is presented, together with the luminescence properties for the Tm^{3+}-doped GGG samples. The lanthanide ions can easily enter as dopants in the GGG lattice structure as these ions have nearly the same ionic size of the Gd^{3+} ions. The incorporation of Ln^{3+} ions in the GGG lattice has been addressed by some of us in a previous paper [37]. For a detailed structural characterization we focused on the two more concentrated doped samples, as the possible changes in the garnet structure should be more evident. The Pr^{3+}- and Tm^{3+}-doped samples have been chosen as representative of the larger Ln^{3+} ions at the beginning of the lanthanide series and of the smaller ions at the end, respectively.

One of the aims of this investigation is to identify the phases and to determine the lattice parameters, crystallite dimensions and chemical composition for the nanocrystalline GGG samples. Such investigations were performed using x-ray powder diffraction, electron diffraction and high-resolution electron microscopy. The analysis of the x-ray diffraction patterns was made using the Rietveld method. Compositional measurements were done using energy dispersive x-ray (EDX) spectroscopy coupled to a scanning electron microscope or a transmission electron microscope. The spectroscopic properties of the Tm^{3+}-doped GGG samples were studied using laser-excited luminescence spectroscopy. The optical spectroscopy of the Pr^{3+}-doped samples will be the subject of a separate paper [38].

2. Experimental details

2.1. Synthesis

GGG nanocrystals, undoped and doped with Pr^{3+} and Tm^{3+} ions, were synthesized using a solution combustion procedure starting from an aqueous mixture of $(NH_2NH)_2CO$ (98%), $Gd(NO_3)_3{\cdot}6H_2O$ (99.99%), $Ga(NO_3){\cdot}3H_2O$ (99.999%) and $Ln(NO_3)_3{\cdot}6H_2O$ (99.9%) (Ln = Pr; Tm). GGG nanocrystalline samples containing 10% of Pr^{3+} ions and 1, 5, 10% of Tm^{3+} ions with respect to Gd^{3+} were prepared. Details of this preparation method can be found in [13, 14]. After the combustion, the powders were annealed in air for 1 h at 500 °C in order to decompose the residual carbohydrazide and nitrate ions. The samples were subsequently heat treated in air at 800 °C for 72 h.

2.2. Structural characterization

The morphology, local composition and microstructure of the GGG samples were studied by x-ray diffraction, electron microscopy and EDX analysis.

The x-ray diffraction (XRD) patterns were measured on a Thermo ARL X'TRA powder diffractometer (Cu Kα radiation, $\lambda = 1.5418$ Å, Bragg–Brentano geometry, Peltier-cooled CCD detector). XRD data were collected at room temperature over the 10°–100° 2θ range with steps of 0.02°. XRD patterns were analysed by the Rietveld method [39, 40] using the RIETAN-98 program [41]. The fractional coordinates of GGG (space group $Ia\bar{3}d$ [42]) and $Ca_3(Al_{0.8}Fe_{0.2})_2(SiO_4)_3$ (space group $Fddd$ [3]) were used as initial parameters. The

background, profile and unit-cell parameters were refined. Atomic coordinates and atomic displacement parameters were not refined.

Scanning electron microscopy (SEM) observations were performed with a Jeol JEM-5510 equipped with an INCA x-ray microanalysis unit. The composition of the samples was determined by x-ray energy-dispersion spectrometry (EDS) acquiring a spectrum for 600 s (live time) at the accelerating voltage of 30 kV. For this analysis powders were cold-pressed into pellets of 3 mm diameter under a load of about 2 tonnes of pressure and then left uncoated.

Transmission electron microscopy (TEM) was used to obtain information about the structure and size distribution of the nanoparticles. Electron diffraction and EDX analysis were performed on a Philips CM20 microscope, operating at 200 kV and equipped with a LINK-2000 EDX attachment. High-resolution electron microscopy (HREM) observations were made on a Jeol 4000EX electron microscope. TEM specimens were prepared by dispersing the finely crushed powdered sample in pure ethanol, exposing the solution to ultrasonic vibrations for about 10 min and then depositing a drop of solution on a holey carbon film grid. The CrystalKitX and MacTempas software packages (software for High Resolution Electron Microscopy, Total Resolution, 20 Florida Ave., Berkeley, CA, USA) were used to simulate electron diffraction patterns and HREM images.

2.3. Luminescence spectroscopy

The room-temperature emission spectra and decay curves of the Tm^{3+}-doped GGG nanocrystalline samples were measured upon excitation with the third harmonic (at 355 nm) of the fundamental radiation of a Quanta System SYL201 Nd–YAG pulsed laser. The emission radiation was dispersed with a Jobin Yvon HR450 half-metre monochromator equipped with a 150 lines mm^{-1} grating. A Jobin Yvon Spectra One air-cooled CCD device was employed to record the emission spectra. A water-cooled Hamamatsu GaAs photomultiplier and a Le Croy Waverunner LT342 digital oscilloscope were used to obtain the emission decay curves.

3. Results and discussion

3.1. Composition determination

After synthesis, the GGG powders consist of agglomerates with an irregular shape and a size ranging from a few tens of microns to a few millimetres. Before observation in the electron microscope, the powders were lightly ground in a mortar to obtain smaller agglomerates.

The average composition of the undoped and 10% Pr^{3+}- and Tm^{3+}-doped GGG samples was determined by energy-dispersive x-ray (EDX) spectroscopy in a scanning electron microscope. The EDX spectra, shown in figure 1, confirm the lanthanide doping of the GGG samples and show that the elemental ratio Gd/Pr $\approx$ 8.6 is close to that expected for a solid solution of $Gd_{2.7}Pr_{0.3}Ga_5O_{12}$ composition. For the Tm^{3+}-doped sample it was more difficult to obtain accurate results by EDX, due to the overlap of some Tm and Gd peaks.

Using the EDX mapping technique it was also possible to verify the homogeneity of the samples. Elemental maps

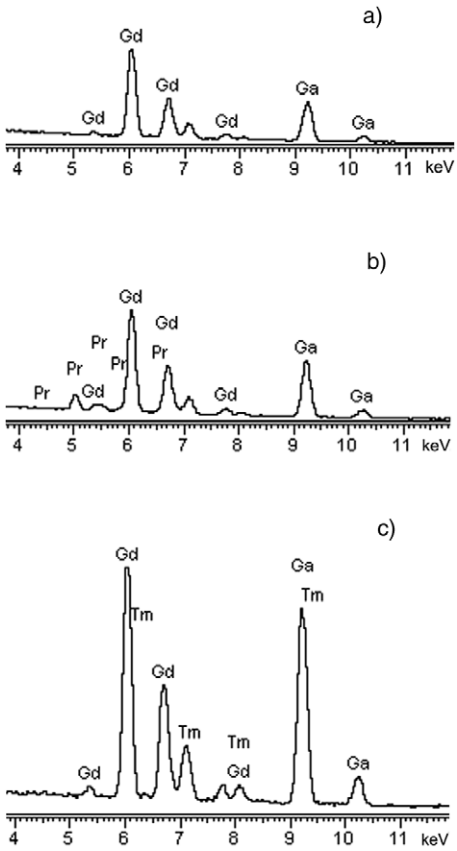

Figure 1. EDX spectra of undoped $Gd_3Ga_5O_{12}$ (a) and $Gd_3Ga_5O_{12}$ doped by lanthanides (Pr^{3+} (b), Tm^{3+} (c)).

of Gd, Ga, O, Pr and Tm show uniform density, indicating good homogeneous distribution of praseodymium and thulium throughout the material.

EDX measurements performed in the TEM apparatus and using the classical composition determination software, show a Ga/Gd ratio for the undoped GGG nanocrystalline sample of 1.44 $\pm$ 0.06 (the stoichiometric Ga/Gd ratio is 1.67). The elemental analysis gives 59 $\pm$ 2 at.% for Ga and 41 $\pm$ 2 at.% for Gd. These results slightly deviate from the stoichiometric 62.5 at.% and 37.5 at.% for Ga and Gd, respectively. Therefore, the element contents in a commercial $Gd_3Ga_5O_{12}$ sample (ALDRICH, 99.9%) were determined as references. The experimental EDX results for the commercial GGG gave 61 $\pm$ 1 at.% for Ga and 39 $\pm$ 1 at.% for Gd, with a Ga/Gd ratio of 1.56 $\pm$ 0.03. The element content values found for the commercial sample are closer to the ideal stoichiometry than for the nanocrystalline GGG samples, that appear to be slightly richer in Gd than predicted from the formula.

3.2. X-ray diffraction study

Parts of the XRD pattern from 10° to 65° and from 38° to 48° for undoped GGG are shown in figure 2. The first analysis of the XRD pattern for GGG by the Rietveld method was done in the model of a single-phase cubic garnet. As shown in figure 2(a), each reflection of the GGG cubic phase on the XRD patterns is accompanied by an asymmetric peak shifted to the

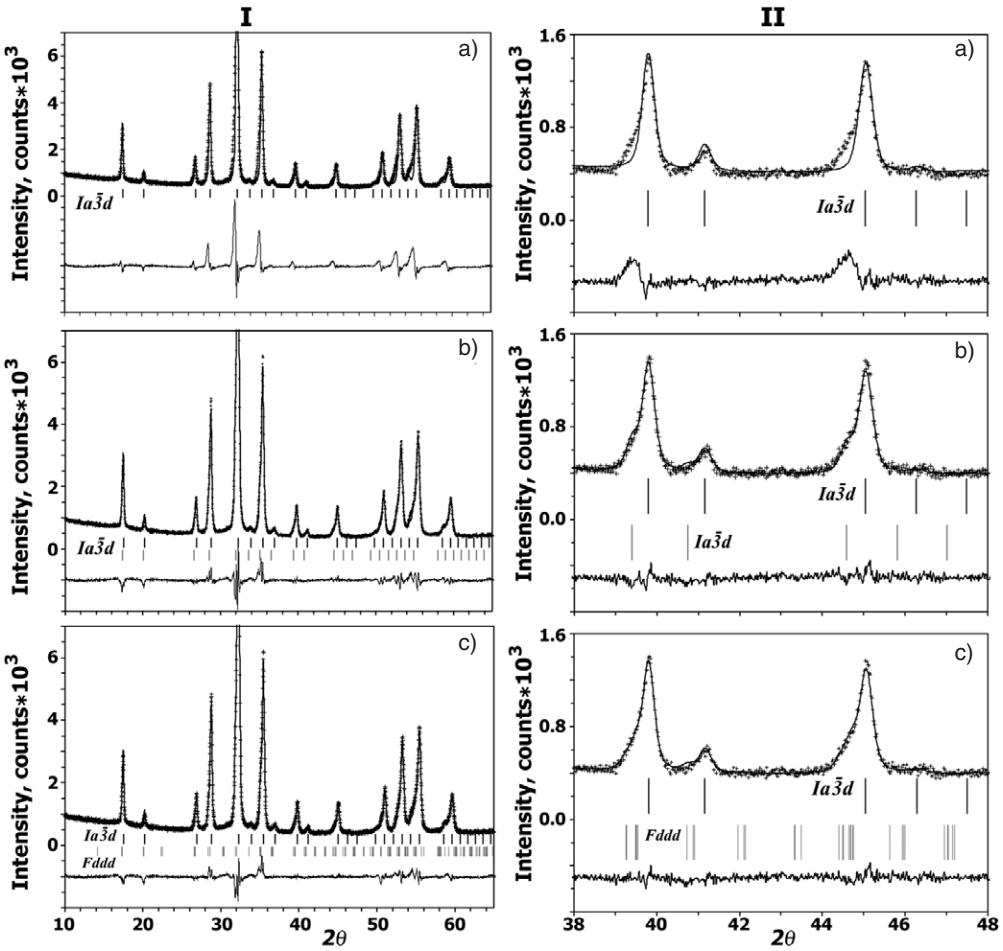

Figure 2. Parts (I—from 10° to 65° and II—from 38° to 48°) of the observed (crosses), calculated (solid line) and difference XRD patterns for undoped $Gd_3Ga_5O_{12}$: (a) model with one single-phase cubic garnet; (b) model with two cubic phases; (c) model with one cubic phase and one orthorhombic distorted phase. Tick marks denote the peak positions of possible Bragg reflections of the different phases.

left of it. Rietveld difference patterns (figure 2(a)) show a clear evidence of the presence of a second garnet-type phase. There are two possible models for the two-phase refinement: (i) two cubic phases with a different unit-cell parameter; (ii) a cubic and a distorted garnet-type phase. The GGG lattice is body-centred cubic (space group $Ia\bar{3}d$) with a lattice parameter of ≈1.24 nm. The formation of a second cubic phase with a larger unit cell than GGG might be explained in terms of the formation of a solid solution $Gd_{3+x}Ga_{5-x}O_{12}$ with a statistical distribution of Gd^{3+} and Ga^{3+} on the octahedral site. It should be noted that a heat treatment at 1450 °C for 6 h of the GGG:1 mol% Ho, with a second garnet-type phase, leads to the formation of a pure GGG cubic phase [36]. The fit for this model with the experimental data can be seen in figure 2(b). A slightly better agreement between the observed and the calculated patterns, however, occurs for a model with a cubic ($Ia\bar{3}d$) and an orthorhombic ($Fddd$) garnet-type phase with unit-cell parameters $a_o \approx a_c \times \sqrt{2}$, $b_o \approx a_c$, $c_o \approx a_c \times \sqrt{2}$, where a_o, b_o, c_o and a_c are the unit-cell parameters of orthorhombic and cubic phases (figure 2(c)), respectively. Such an orthorhombic phase might be metastable and could transform to the cubic garnet phase at higher temperatures. Bazzoni *et al* [22] recently observed various metastable phases in nanocrystalline GGG prepared with the co-precipitation technique. The type of synthesis of the nanosized material and the post-synthesis treatments, such as annealing temperature or mechanical milling, can be responsible for the appearance of various metastable GGG phases. The experimental/refinement conditions, final *R* factors, and lattice parameters for all models of the Rietveld refinement are summarized in table 1. A final decision between two cubic phases or a cubic and a distorted cubic phase cannot be made from the XRD data only. TEM will have to provide the answer (see below).

XRD patterns for the lanthanide (Pr^{3+}, Tm^{3+})-doped GGG are very similar to the XRD pattern for undoped GGG. Each reflection of the GGG 10 mol% Pr (Tm) cubic phase in the XRD patterns is also characterized by an asymmetric peak. The unit-cell parameters of undoped GGG and GGG doped with the lanthanide ions after Rietveld refinement are given in table 2. The unit-cell parameter changes with the lanthanide doping and the volume of the unit cell increases for the Pr-doped sample and decreases for the Tm-doped sample. A similar dependence on the doping is observed for the unit-cell parameter of the cubic phase and agrees with the size of the Pr^{3+} and Tm^{3+} ions with respect to the host Gd^{3+} cations.

Table 1. Crystallographic data, experimental conditions, and refinement results for undoped $Gd_3Ga_5O_{12}$.

Experimental conditions					
Diffractometer			Thermo ARL X'TRA		
Radiation λ (Å)			Cu Kα (1.5418)		
Temperature (°C)			24		
2θ range (deg)			10–110		
Step scan increment (2θ)			0.02		
I_{max}			14 694		
Refinement results					
	Single-phase model	Two-phase models			
		I phase	II phase	I phase	II phase
Space group	$Ia\bar{3}d$	$Ia\bar{3}d$	$Ia\bar{3}d$	$Ia\bar{3}d$	$Fddd$
Z	8	8	8	8	16
Unit-cell parameters					
a (nm)	1.241 14(2)	1.239 78(2)	1.251 53(5)	1.239 52(3)	1.755(2)[a]
b (nm)					1.2572(1)
c (nm)					1.763(2)[b]
V (nm^3)	1.9119(1)	1.9056(1)	1.9603(1)	1.9044(1)	3.911(5)
Phase ratio (I phase/II phase)		0.795/0.205		0.717/0.283	
Reliability factors (%)					
R_{WP}, R_P	11.65, 8.80	6.42, 5.01		6.07, 4.58	
R_I, R_F	3.57, 1.64	1.53, 0.60	1.61, 0.65	1.46, 0.79	1.56, 0.81

[a] $-a/\sqrt{2} \approx 1.241$ nm.

[b] $c/\sqrt{2} \approx 1.247$ nm.

Table 2. Unit-cell parameters for $Gd_3Ga_5O_{12}$ and $Gd_3Ga_5O_{12}$ doped by lanthanide (Pr, Tm) (space groups $Ia\bar{3}d$ and $Fddd$) after Rietveld refinements.

Compound	r_{VIII} (Ln), (Å) [53]	Model	a (nm)	b (nm)	c (nm)	V (nm^3)
GGG	1.06	1 phase	1.241 14(2)			1.9119(1)
		2 phases	1.239 52(3)			1.9044(1)
			1.755(2)	1.2572(1)	1.763(2)	3.911(5)
GGG	1.14	1 phase	1.243 02(6)			1.9206(2)
10 mol% Pr		2 phases	1.241 48(4)			1.9134(1)
			1.7664(3)	1.2473(3)	1.7856(2)	3.934(1)
GGG	0.99	1 phase	1.237 63(5)			1.8957(1)
10 mol% Tm		2 phases	1.237 22(2)			1.8938(1)
			1.7608(2)	1.2439(2)	1.7785(2)	3.895(1)

Table 3. Results of EDX quantitative analysis in the transmission electron microscope for undoped $Gd_3Ga_5O_{12}$ and $Gd_3Ga_5O_{12}$ doped with 10 mol% Pr and Tm. Average values with errors estimated as one standard deviation are reported.

at.% sample	Ga K	Gd L	Pr L	Tm L	x
$Gd_{3-x}Pr_xGa_5O_{12}$	59 ± 2	37 ± 2	4.2 ± 0.5		0.31 ± 0.05
$Gd_{3-x}Tm_xGa_5O_{12}$	59 ± 2	37 ± 2		4.3 ± 0.5	0.31 ± 0.04
$Gd_3Ga_5O_{12}$	59 ± 2	41 ± 2			

3.3. Electron microscopy study

The elemental composition of undoped GGG and lanthanide-doped GGG was confirmed by EDX analysis in the transmission electron microscope on different crystallites; at the same time, the structure was verified by electron diffraction. The EDX analysis was performed with the Ga K, Gd L, Pr L and Tm L lines, taking measurements for at least 25 different crystallites for each sample. The results of the EDX quantitative analysis for undoped and doped $Gd_3Ga_5O_{12}$ samples are listed in table 3.

TEM observations show that agglomerates are composed of nanosized crystallites with an irregular form and various dimensions, ranging from 30 to 100 nm (figure 3). The voids present are the result of the very rapid combustion reaction during synthesis.

The cubic structure of $Gd_3Ga_5O_{12}$ was confirmed for all samples by analysing the electron diffraction (ED) patterns. The ring pattern (inset in figure 3) indicates that our material is polycrystalline. The grainy rings are related to the fact that the constituent crystallites have a size of 30 nm or more. The ring pattern could be indexed as the cubic $Gd_3Ga_5O_{12}$ structure: in figure 3, for clarity, only the most intense rings are indexed.

The local crystal structure was investigated by analysing single-domain ED patterns and the corresponding high-resolution images. The model used for the image simulations is the $Gd_3Ga_5O_{12}$ structure with space group O_h^{10} ($Ia\bar{3}d$) and $a \approx 1.24$ nm. Single-domain ED patterns obtained for the main zones, $[001]^*$, $[0\bar{1}1]^*$ and $[11\bar{1}]^*$, are shown in figure 4. All ED patterns are completely indexed on a cubic unit cell with lattice parameter around 1.24 nm, in agreement with the data

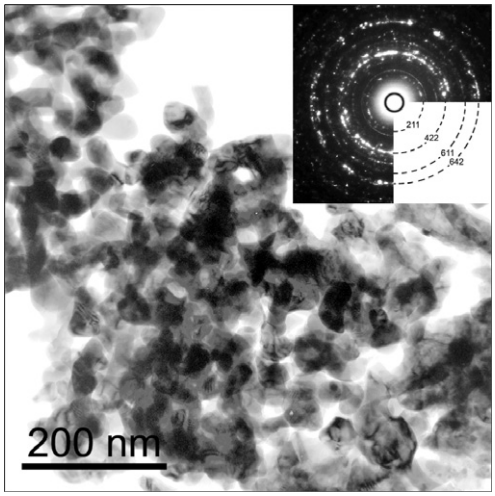

Figure 3. TEM image and corresponding electron diffraction ring pattern of undoped $Gd_3Ga_5O_{12}$. Only the most intense rings are indexed.

from x-ray powder diffraction (table 2). Using TEM, however, we could not observe any evidence for an orthorhombic garnet-type phase as eventually suggested from the x-ray diffraction analysis. No spot splitting, and no superlattice reflections were present in any of the patterns. We did, however, notice a slight variability in the lattice parameter between different grains.

The general reflection conditions for the space group $Ia\bar{3}d$ are as follows. hkl: $h + k + l = 2n$, $0kl$: k, $l = 2n$, hhl: $2h + l = 4n$, $h00$: $h = 4n$, where h, k and l are permutable. ED patterns of $[001]^*$ and $[11\bar{1}]^*$ zones exhibit reflections with indices $h00 \neq 4n$ (200) and hhl, $2h + l \neq 4n$ (110) due to double diffraction. For the $[0\bar{1}1]^*$ zone these extra reflection do not occur, as double diffraction conditions are not present.

In order to check the quality of the nanocrystals, we analysed a number of them with HREM. The nanocrystals proved to be stable under the electron beam. However, we worked very fast, using the smallest beam intensity, and controlling any possibly e-beam transformation (or damage) by taking the series of images and comparing the first and the last image. In figure 5, an HREM image of one Pr-doped GGG nanocrystal along the $[001]^*$ direction is shown. The surface is free of defects and without any amorphous layer. The structure can be interpreted in terms of cation and oxygen columns where brighter dots correspond to Gd and Ga atomic columns (and/or Pr). Computer simulations made for the trial model, in which dopant ions of Pr^{3+} enter the structure by replacing Gd^{3+} ions randomly, match the experimental HREM images well. No differences in intensity are observed, in agreement with the fact that the Pr doping is homogeneous. This is also consistent with the absence of diffuse intensity in the ED patterns. No cation ordering is observed, but EDX analysis in the TEM confirmed the presence of the Ln (Ln = Pr, Tm) dopant in the expected proportion. The results of quantitative EDX analysis are presented in table 3.

For doped samples the atomic concentration ratio of Ga^{3+}/Gd^{3+} ions is increased (1.62) compared to that observed in undoped $Gd_3Ga_5O_{12}$ (1.44) (see table 3). This is another indication that Pr^{3+} and Tm^{3+} indeed entered the structure, mainly substituting Gd^{3+} ions. On the other hand, the

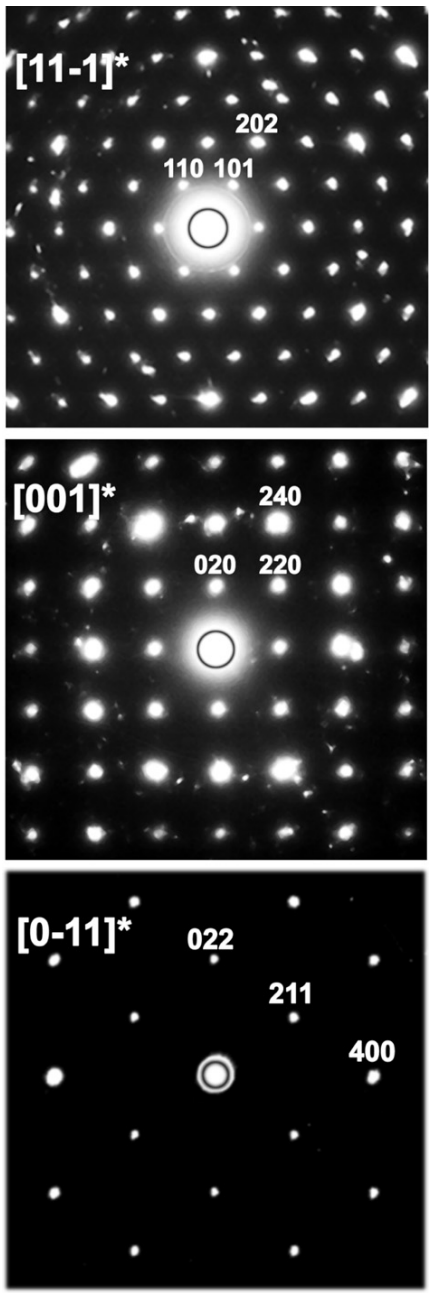

Figure 4. ED patterns of the undoped $Gd_3Ga_5O_{12}$ along the $[001]^*$, $[011]^*$ and $[111]^*$ zone axes.

concentration ratio Gd^{3+}/Ln^{3+} (Ln = Pr, Tm) is quite stable and close to the ideal value of 9. This can be used as a quantitative confirmation that a solid solution with the stoichiometry of $Gd_{2.7}Ln_{0.3}Ga_5O_{12}$ and a uniform dopant distribution was effectively obtained.

3.4. Luminescence

The room-temperature luminescence spectrum for the 1% Tm^{3+}-doped GGG nanocrystalline sample was obtained under direct excitation in the $^1D_2$ level of Tm^{3+} ion with 355 nm radiation (figure 6). The luminescence spectrum is dominated by strong emission bands located around 460 nm, which can be assigned to transitions between the Stark components of

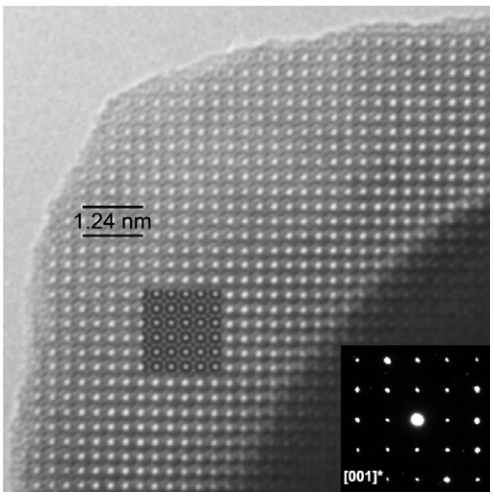

Figure 5. HREM image and corresponding ED pattern for Pr^{3+}-doped $Gd_3Ga_5O_{12}$ along the [001]* zone. The simulated image for a focus value of 80 nm and a thickness of 2.5 nm is shown as an inset.

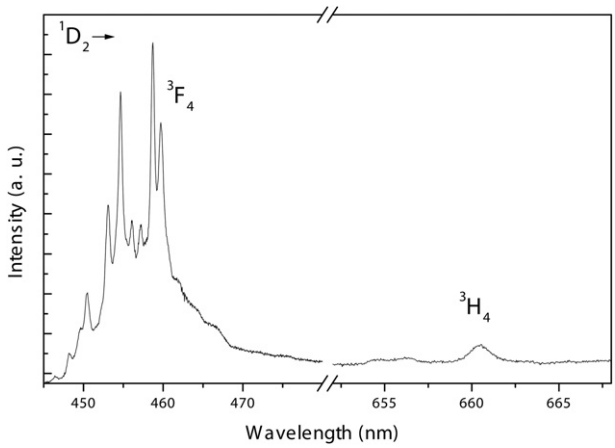

Figure 6. Room-temperature luminescence spectrum of the 1% Tm^{3+}-doped GGG sample ($\lambda_{exc} = 355$ nm).

the $^1D_2$ and $^3F_4$ energy levels of the Tm^{3+} ion [43, 44]. From figure 6 it is evident that the transitions are not fully resolved due to broadening of the emission bands which overlap each other. Luminescence bands due to the $^1D_2 \rightarrow {}^3F_4$ transition were already observed for Tm^{3+}-doped GGG single crystals [44] and for other garnets, such as yttrium scandium aluminium garnet (YSAG), lutetium aluminium garnet (LuAG) or yttrium aluminium garnet (YAG) [45, 46]. A weaker emission band is also observed at about 660 nm, which can be assigned to the $^1D_2 \rightarrow {}^3H_4$ transition [44]. Very weak features presumably due to the $^3H_4 \rightarrow {}^3H_6$ transition are observed around 800 nm (not shown).

The room-temperature luminescence decay curves for the 1, 5 and 10% Tm^{3+}-doped nanocrystalline samples are shown in figure 7. The decay curves show a non-exponential behaviour for all the Tm^{3+}-doped GGG samples. As evidenced from the x-ray diffraction patterns, two slightly different garnet phases have been found for the Tm^{3+}-doped GGG samples under investigation. Therefore, the non-exponential behaviour

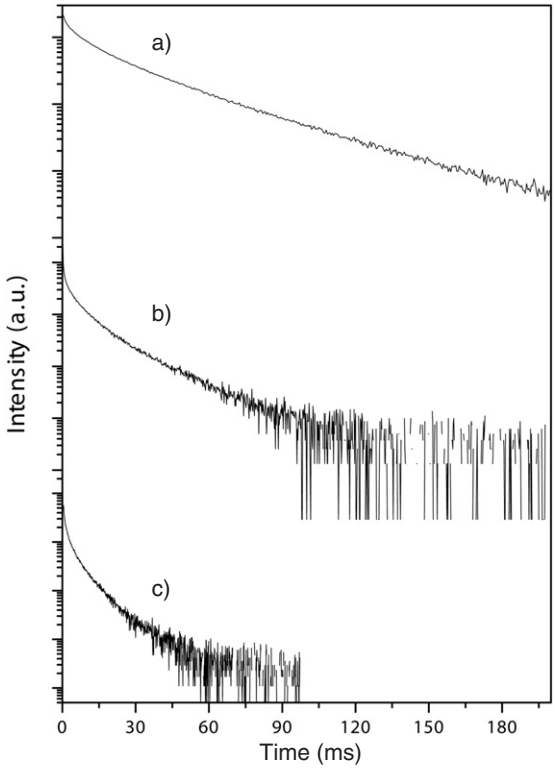

Figure 7. Room-temperature luminescence decay curves for the 1% (a), 5% (b), and 10% (c) Tm^{3+}-doped GGG samples.

of the luminescence decays could be due to the presence of more than one emitting Tm^{3+} sites, accommodated in the two above-mentioned garnet phases. On the other hand, a different explanation could also be invoked to account for the non-exponential behaviour. Due to the nanocrystalline nature of the samples, a relevant percentage of the dopant Tm^{3+} lanthanide ions lies on the surface of the nanoparticle. The crystal field around dopant ions located on or near the surface could be different from that existing around dopant ions in the bulk of the nanoparticle. This could give rise to different transition probabilities resulting in a non-exponential behaviour of the emission decay curves. Besides, it is evident from figure 7 that the luminescence decays shorten continuously on passing from the 1% to the 5% and to the most concentrated 10% Tm^{3+}-doped GGG samples. From the experimental data, we have calculated the effective decay time τ_{eff} using the equation [47]

$$\tau_{eff} = \frac{\int_0^\infty t I(t)\,dt}{\int_0^\infty I(t)\,dt}, \qquad (1)$$

where $I(t)$ represents the luminescence intensity at time t corrected for the background and the integrals are evaluated in a range $0 < t < t_{max}$, where $t_{max} \gg \tau_{eff}$. The obtained τ_{eff} values of the $^1D_2$ level of the Tm^{3+} ion for the samples under investigation are reported in table 4. It is clearly evident that the effective decay time decreases on increasing the dopant concentration in the GGG host. This behaviour strongly suggests that a non-radiative cross-relaxation (CR) process between the Tm^{3+} ions is present. Taking into account the energy levels of the Tm^{3+} ion in the GGG single

Table 4. Room-temperature effective decay times τ_{eff} of the $^1D_2$ level of Tm^{3+} in doped GGG nanocrystalline samples ($\tau_{exc} = 355$ nm).

Nanocrystalline GGG:Tm^{3+} (%)	τ_{eff} (μs)
1	30.9
5	10.8
10	6.5

crystal [44] the most likely CR mechanism is $(^1D_2, {}^3H_6) \rightarrow (^3H_4, {}^3F_2)$. This process is non-resonant, but the mismatch (about 350 cm^{-1}) can be easily bridged by the emission of one phonon. In fact, the Raman spectrum of an undoped nanocrystalline GGG sample shows a strong band peaked at a Raman shift of about 350 cm^{-1} [38]. The CR process of course becomes more efficient in the most concentrated sample, which also shows the shorter τ_{eff} value. In the 5% and 10% samples, the relaxation of the $^1D_2$ level is also enhanced by energy migration among the donor levels [48]. It is important to remark that cross-relaxation processes causing the quenching of different excited states have been observed for Tm^{3+}-doped GGG single crystals [49], even in more diluted samples (0.5% doping level).

The Judd–Ofelt parameters for the Tm^{3+} ion in the GGG host were obtained by Brenier *et al* [50] and turned out to be $\Omega_2 = 1.85 \times 10^{-21}$ cm^2, $\Omega_4 = 9.61 \times 10^{-21}$ cm^2, $\Omega_6 = 7.36 \times 10^{-21}$ cm^2. The average refractive index of GGG is 1.965 [51]. Using the Judd–Ofelt parameters and this value, the radiative lifetime τ_{rad} for the $^1D_2$ level results to be 75 μs. The percentage quantum efficiency η% of the $^1D_2 \rightarrow {}^3F_4$ emission, obtained with the formula

$$\eta\% = 100\tau_{eff}/\tau_{rad}, \qquad (2)$$

is 44, 15 and 9 for the 1, 5 and 10% Tm^{3+}-doped nanocrystalline GGG samples, respectively. It is worth noting that the energy gap between the $^1D_2$ and the next lower lying $^1G_4$ level is approximately 6000 cm^{-1}. Considering that the phonon energy cutoff for the GGG host is about 600 cm^{-1} [26], approximately 10 phonons would be required to bridge the energy gap between the $^1D_2$ and the $^1G_4$ levels. For this reason, the multiphonon transition probability from the $^1D_2$ level is very low and therefore the $^1D_2$ level can be depopulated by photon emission or via cross-relaxation processes. Since the effective decay times for all the nanocrystalline samples are significantly lower than the radiative lifetime, we can reasonably conclude that cross-relaxation processes are present even for the most diluted nanocrystalline sample, contributing to the non-exponential decay behaviour.

4. Conclusions

This work presents a structural and morphological investigation of nanocrystalline $Gd_3Ga_5O_{12}$ samples, undoped and doped with Pr^{3+} or Tm^{3+} rare earth ions. The analysis by the Rietveld method of XRD patterns of GGG powders (undoped and doped with Pr^{3+} or Tm^{3+}) reveals the existence of two garnet-type phases. The better agreement between the observed and the calculated patterns was found for a model with a cubic (space group $Ia\bar{3}d$, usual GGG structure) and a garnet distorted orthorhombic structure. Using electron diffraction we did not find any evidence for an orthorhombic phase and we therefore conclude that the material consists of two cubic phases with a slightly different lattice parameter. One might argue though that the orthorhombic phase is a non-equilibrium phase formed during propellant synthesis and that under the electron beam this phase is transformed into a cubic phase. We have tried to avoid transformation by working under minimum illumination conditions, but we could never find evidence for the orthorhombic phase. We detected a change of cell parameter with lanthanide doping due to the difference in size between the dopant and the host ions. The volume of the unit cell of all phases increases for the Pr-doped sample and decreases for the Tm-doped sample. A similar dependence on the doping is observed for the unit-cell parameter of the cubic phase. This was a first confirmation that the dopants enter into the GGG structure.

The electron microscopy technique directly images the powder agglomerates and shows that they are constituted of aggregated single-crystal particles with an irregular shape and a size distribution ranging from 30 to 100 nm. HREM images, for undoped and doped samples, show a stable, well-ordered structure of $Gd_3Ga_5O_{12}$ crystals without any defect or cation ordering. The presence of the dopants is confirmed by EDX microanalysis. The observed HREM images and ED patterns are in good agreement with the simulated ones for the structural model where dopant atoms are randomly distributed on the Gd^{3+} atomic positions. The results for the Pr^{3+}-doped nanocrystalline GGG agree with the results obtained from EXAFS spectroscopy on the same material [52]. As a conclusion, we have found that the solution propellant method is able to produce very good solid solutions of $Gd_3Ga_5O_{12}$, in nanocrystalline form, with a homogeneous distribution of the lanthanide dopants. Results of quantitative EDX analysis show that a solid solution with stoichiometry $Gd_{\approx 2.7}Ln_{\approx 0.3}Ga_5O_{12}$ (Ln = Pr or Tm) was effectively obtained for 10 mol% praseodymium and thulium-doped $Gd_3Ga_5O_{12}$ samples.

The luminescence spectrum of the 1% Tm^{3+}-doped nanocrystalline GGG sample is dominated by a strong emission in the blue region around 460 nm after excitation in the ultraviolet (at 355 nm). The emission decay curves for the Tm^{3+}-doped GGG samples show a non-exponential behaviour which can be explained by the presence of more than one phase in which the Tm^{3+} is accommodated, by the presence of cross-relaxation processes, and by surface effects. The presence of these processes decreases the effective decay time of the $^1D_2$ energy level and the quantum efficiency of the $^1D_2 \rightarrow {}^3F_4$ emission of the Tm^{3+} ion on increasing the dopant concentration in the samples under investigation. On the other hand, the quantum efficiency of the $^1D_2 \rightarrow {}^3F_4$ emission for the most diluted sample is relatively high (around 50%), suggesting that the present Tm^{3+}-doped GGG materials could be promising as blue luminophors for applications in which nanocrystalline light-emitting materials are required.

Acknowledgments

This work was performed within the framework of the Belgian IAP5-01 project and the 2003 PRIN/Cofin contract of the

Italian Ministry for University and Research (MURST). Dr Daniele Falcomer from the University of Verona is gratefully acknowledged for his help in measuring the luminescence spectrum and emission decay curves.

References

[1] Abrahams S C and Geller S 1958 *Acta Crystallogr.* **11** 437
[2] Aubry A, Dusausoy Y, Laffaille A and Protas J 1969 *Bull. Soc. Fr. Miner. Cristallogr.* **92** 126
[3] Takeuchi Y, Haga N, Umizu S and Sato G 1982 *Z. Kristallogr.* **158** 53
[4] Eppler W R and Kryder M H 1995 *J. Phys. Chem. Solids* **56** 1479
[5] Aichele T, Lorenz A, Hergt R and Görnert P 2003 *Cryst. Res. Technol.* **38** 575
[6] Ibrahim N B, Edwards C and Palmer S B 2000 *J. Magn. Magn. Mater.* **220** 183
[7] Chénais S, Druon F, Balembois F, Georges P, Brenier A and Boulon G 2003 *Opt. Mater.* **22** 99
[8] Kir'yanov A V, Aboites V, Belovolov A M, Timoshechkin M I, Belovolov M I, Damzen M J and Minassian A 2002 *Opt. Express* **10** 832
[9] McKittrick J, Shea L E, Bacalski C F and Bosze E J 1999 *Displays* **19** 169
[10] Talin A A, Dean K A and Jaskie J E 2001 *Solid State Electron.* **45** 963
[11] Hunt C E and Chakhovskoi A G 1997 *J. Vac. Sci. Technol.* B **15** 516
[12] Fukaya S, Adachi K, Obara M and Kumagai H 2001 *Opt. Commun.* **187** 373
[13] Ye T, Guiwen Z, Weiping Z and Shangda X 1997 *Mater. Res. Bull.* **32** 501
[14] Tessari G, Bettinelli M, Speghini A, Ajò D, Pozza G, Depero L E, Allieri B and Sangaletti L 1999 *Appl. Surf. Sci.* **144/145** 686
[15] Shikao S and Jiye W 2001 *J. Alloys Compounds* **327** 82
[16] Ramanathan S, Kakade M B, Roy S K and Kutty K K 2003 *Ceram. Int.* **29** 477
[17] Ekambaram S and Patil K C 1995 *J. Alloys Compounds* **217** 104
[18] Hreniak D and Strek W 2002 *J. Alloys Compounds* **341** 183
[19] Qiu F, Pu X, Li J, Liu X, Pan Y and Guo J 2005 *Ceram. Int.* **31** 663
[20] Sharma P K, Jilavi M H, Schmidt H and Varadan V K 2000 *Int. J. Inorg. Mater.* **2** 407
[21] Zhao G, Li T, He X and Xu J 2002 *Mater. Lett.* **56** 1098
[22] Bazzoni M, Bettinelli M, Daldosso M, Enzo S, Serra F and Speghini A 2005 *J. Solid State Chem.* **178** 2301
[23] Wyss Chr P *et al* 1999 *J. Lumin.* **82** 137
[24] Brenier A, Courrol L C, Madej C and Boulon G 1994 *Phys. Rev.* B **49** 881
[25] Carazo-Salas R, Murday R, Proulx P P, Karbo P, Cormier G and Capobianco J A 1996 *Opt. Mater.* **6** 203
[26] Vetrone F, Boyer J C, Capobianco J A, Speghini A and Bettinelli M 2003 *J. Phys. Chem.* B **107** 10747
[27] Boyer J C, Vetrone F, Capobianco J A, Speghini A, Zambelli M and Bettinelli M 2004 *J. Lumin.* **106** 263
[28] Naccache R, Vetrone F, Boyer J C, Capobianco J A, Speghini A and Bettinelli M 2004 *J. Nanosci. Nanotechnol.* **4** 1025
[29] Boyer J C, Vetrone F, Capobianco J A, Speghini A and Bettinelli M 2004 *Chem. Phys. Lett.* **390** 403
[30] Mita Y, Togashi M and Yamamoto H 2000 *J. Lumin.* **87–89** 1026
[31] Sharma P K, Jilavi M H, Nass R and Schmidt H 1999 *J. Lumin.* **82** 187
[32] Lopez O A, McKittrick J and Shea L E 1997 *J. Lumin.* **71** 1
[33] Williams K D, Yuan H and Tissue M B 1999 *J. Lumin.* **83/84** 297
[34] Allieri B, Depero L E, Marino A, Sangaletti L, Caporaso L, Speghini A and Bettinelli M 2000 *Mater. Chem. Phys.* **66** 164
[35] Vaqueiro P and López-Quintela M A 1998 *J. Mater. Chem.* **8** 161
[36] Krsmanović R, Polizzi S and Canton P 2005 *Mater. Sci. Forum* **494** 143
[37] Maglia F, Buscaglia V, Gennari S, Ghigna P, Dapiaggi M, Speghini A and Bettinelli M 2006 *J. Phys. Chem.* B **110** 6561
[38] Naccache R, Vetrone F, Capobianco J A, Speghini A and Bettinelli M 2007 in preparation
[39] Rietveld H M 1969 *J. Appl. Crystallogr.* **2** 65
[40] Izumi F 1993 *The Rietveld Method* (New York: Oxford University Press) chapter 13
[41] Kim Y I and Izumi F 1994 *J. Ceram. Soc. Japan* **102** 401
[42] Dukhovskaya E L, Saksonov Y G and Titova A G 1973 *Neorg. Mater.* **9** 809
Sawada H 1997 *J. Solid State Chem.* **132** 300
[43] Brenier A, Garapon C, Madej C, Pédrini C and Boulon G 1994 *J. Lumin.* **62** 147
[44] Lupei A, Lupei V, Grecu S, Tiseanu C and Boulon G 1994 *J. Appl. Phys.* **75** 4652
[45] Gruber J B, Seltzer M D, Hills M E, Stevens S B and Morrison C A 1993 *J. Appl. Phys.* **73** 1929
[46] Cicillini S A, Pires A M and Serra O A 2004 *J. Alloys Compounds* **374** 169
[47] Nakazawa E 1999 *Phosphor Handbook* (Boca Raton, FL: CRC Press) p 104
[48] Martín I R, Rodríguez V D, Alcalá R and Cases R 1993 *J. Non-Cryst. Solids* **161** 294
[49] Brenier A, Madej C, Pédrini C and Boulon G 1991 *J. Phys.: Condens. Matter* **3** 203
[50] Brenier A, Courrol L C, Pédrini C, Madej C and Boulon G 1994 *Phys. Rev.* B **49** 881
[51] Gill D S, Anderson A A, Eason R W, Warburton T J and Shepherd D P 1996 *Appl. Phys. Lett.* **69** 10
[52] Daldosso M, Falcomer D, Speghini A, Ghigna P and Bettinelli M 2007 *Opt. Mater.* at press (doi:10.1016/j.optmat.2007.05.042)
[53] Shannon R D 1976 *Acta Crystallogr.* A **32** 751